

PAPER • OPEN ACCESS

Machine learning approach to force reconstruction in photoelastic materials

To cite this article: Renat Sergazinov and Miroslav Kramár 2021 *Mach. Learn.: Sci. Technol.* **2** 045030

View the [article online](#) for updates and enhancements.

You may also like

- [Testing inversion algorithms against experimental data: inhomogeneous targets](#)
Kamal Belkebir and Marc Saillard
- [Step By Step Process for Formulating a DFN Model for a Lithium Ion Full Cell Battery](#)
Gregory Dan Chipman and Thomas F. Fuller
- [Oxygen Reduction Reaction Mechanism Study Via the Mean-Field Microkinetic Modeling and Uncertainty Quantification of Model Parameters](#)
Aleksandr Andreevich Kurilovich and Keith J. Stevenson



PAPER

OPEN ACCESS

RECEIVED
12 October 2020REVISED
27 August 2021ACCEPTED FOR PUBLICATION
24 September 2021PUBLISHED
25 October 2021

Original Content from
this work may be used
under the terms of the
[Creative Commons
Attribution 4.0 licence](#).

Any further distribution
of this work must
maintain attribution to
the author(s) and the title
of the work, journal
citation and DOI.



Machine learning approach to force reconstruction in photoelastic materials

Renat Sergazinov^{1,*} and Miroslav Kramár² ¹ Department of Statistics, Texas A & M University, Blocker Building, 155 Ireland St, College Station, TX 77843, United States of America² Department of Mathematics, University of Oklahoma, 601 Elm Avenue, Norman, OK 73019, United States of America

* Author to whom any correspondence should be addressed.

E-mail: mrsergazinov@tamu.edu**Keywords:** convolutional neural networks, granular media, deep learning, image recognition

Abstract

Photoelastic techniques have a long tradition in both qualitative and quantitative analysis of the stresses in granular materials. Over the last two decades, computational methods for reconstructing forces between particles from their photoelastic response have been developed by many different experimental teams. Unfortunately, all of these methods are computationally expensive. This limits their use for processing extensive data sets that capture the time evolution of granular ensembles consisting of a large number of particles. In this paper, we present a novel approach to this problem that leverages the power of convolutional neural networks to recognize complex spatial patterns. The main drawback of using neural networks is that training them usually requires a large labeled data set which is hard to obtain experimentally. We show that this problem can be successfully circumvented by pretraining the networks on a large synthetic data set and then fine-tuning them on much smaller experimental data sets. Due to our current lack of experimental data, we demonstrate the potential of our method by changing the size of the considered particles which alters the exhibited photoelastic patterns more than typical experimental errors.

1. Introduction

Granular materials consist of macroscopic particles, they are ubiquitous in nature and indispensable for a large variety of human activities. Powders and grains play a crucial role in many applications such as agriculture, construction, and chemical industry. As noted in [1], the worldwide annual production of grains and aggregates of various kinds exceeds ten billion metric tons. Moreover, granular materials are the second most manipulated materials in the industry after water. So, understanding the physics of granular materials has a major economic impact.

Despite extensive efforts by scientists, properties of granular systems are still not well understood and some of them remain rather obscure. However, it is well known that the forces in these systems do not propagate uniformly [2–4] but along highly anisotropic filamentary structures called force chains, shown in figure 1. The structure of the force chains is crucial for revealing the underlying physical causes of a wide variety of phenomena [5–9] and plays an important role in determining the mechanical properties of granular systems. The first attempts to experimentally study stresses in granular systems by using photoelastic materials were conducted by Wakabayashi [10] and Dantu [11]. Later, Behringer and Majmudar used photoelastic methods [3] to estimate the forces acting between the particles. We refer the reader to [12] for a comprehensive review of photoelastic methods and their applications to granular materials.

The visualization of the force chains, depicted in figure 1(a), is produced by placing an ensemble of photoelastic particles between two polarizing filters. The fact that the degree of birefringence at each location in the photoelastic material depends on local stress produces a visual pattern of alternating bright and dark fringes, visible in figure 1(b). The precise pattern depends in a complex manner on the orientation of the polarizers, the shape of the material, and how it is stressed. If a circular particle is illuminated by

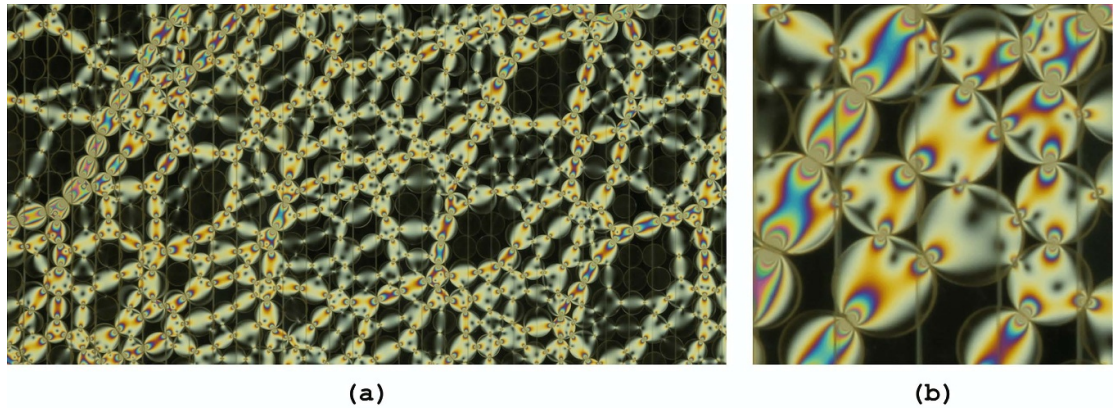


Figure 1. [Courtesy of D. Wang.] (a) An example of a photoelastic response of particles in a sheared system [13] shows that the stresses (forces) in the material propagate along bright filamentary structures called force chains. (b) Detail of the photoelastic pattern on individual particles. Similar patterns are produced by using monochromatic light and they can be used to reconstruct forces acting between the particles.

monochromatic light, then its photoelastic response can be computed from the forces acting on it, see section 2 for more details. However, to determine the forces from the pattern one needs to solve a much more complicated inverse problem.

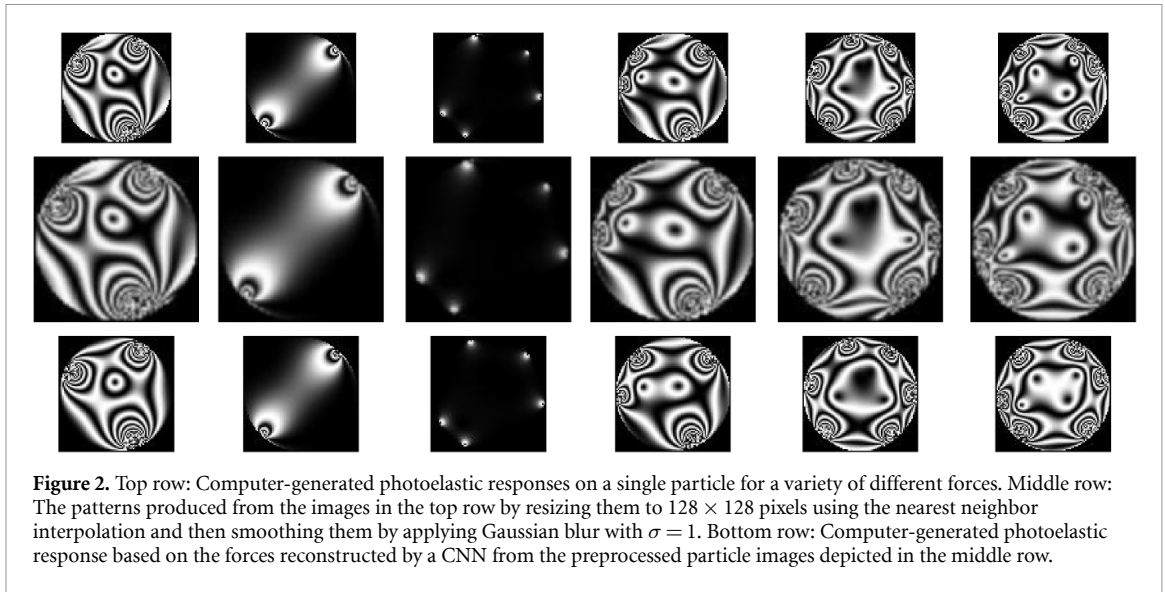
Several computational methods for reconstructing the forces between circular particles were implemented by different groups [14, 15]. While the implementations differ, the algorithms are based on the general ideas presented in [3] and they roughly proceed as follows. First, the positions of the particles are calculated and the force-bearing contacts between them are identified. Then, for each particle the forces acting on it at the force-bearing contacts are guessed. Finally, an optimization algorithm is used to minimize the difference between the experimentally observed pattern exhibited by the particle and the pattern generated from the reconstructed forces.

As mentioned in [12], the positions of the particles can be identified with high accuracy using the Hough transform. However, there might be large discrepancies when it comes to force reconstruction. The reconstructed force between two particles can considerably vary depending on which of the two particles is used for the reconstruction. Moreover, a computationally expensive evaluation of the photoelastic response has to be performed in every iteration of the optimization process. In this paper, we use machine learning to accurately reconstruct the forces acting on a particle from its photoelastic response.

Machine learning algorithms are very efficient for finding and recognizing patterns in complex data [16, 17]. They are extensively used in speech and image recognition as well as predictive analysis, search systems, data visualization, and anomaly detection [17–20]. In particular, convolutional neural networks (CNN) are well suited for the recognition of spatial patterns [17, 21] such as those exhibited by the photoelastic particles.

We show that CNNs produce accurate force reconstruction on synthetic data. This is visually demonstrated by figure 2. The patterns depicted in the top row are computer-generated photoelastic responses of a single particle subject to a variety of different (known) forces acting on it. The images in the middle row are created by first resizing the particles to bring out smaller details and then applying a Gaussian filter to make them look more natural, see section 5 for more details. Note that the corresponding images in the top and bottom row are quite similar. While the precise results are presented in section 6, we just mention that the mean absolute error in predicted positions of the force impact points is around two pixels and the mean absolute percentage error (MAPE) of the predicted force magnitudes is approximately 10%.

To achieve high accuracy of the force reconstruction we experimented with diverse architectures of CNNs. In particular, we considered three different models: VGG19, InceptionResNetV2, and Xception, each pre-trained on the ImageNet data set [22–24]. Despite the high accuracy of our models trained on synthetic data, we cannot guarantee that their predictions on the experimental data would be equally accurate. Unfortunately, training the models directly on experimental data is rather unrealistic because the required number of labeled samples is too large to produce experimentally. To overcome this problem we suggest to pre-train the models on synthetic data and then transfer them to the experimental data by using a relatively small data set. Such a method has already been successfully used for different tasks such as object detection, optical flow estimation, and scene understanding [25–27]. Currently, we do not have the necessary experimental data to prove our claim. Thus, we demonstrate the potential of this approach by transferring our pre-trained model to smaller-sized particles



The paper is organized as follows. Section 2 contains a brief overview of photoelastic theory and explains how the photoelastic response on a circular particle is computed from the forces acting on it. In section 3 we formalize the problem of force reconstruction and summarize earlier works concerned with solving this problem. The machine learning framework for the force reconstruction is discussed in section 4 and the CNN models defined there are trained using the protocol outlined in section 5. Finally, our results are presented in section 6. We conclude the paper with some final remarks in section 7.

2. Photoelastic theory

Photoelastic methods are widely used for quantitative analysis of stress in granular media. In this section, we provide a brief overview of photoelasticity while a detailed treatment can be found in [28]. A comprehensive review of the experimental methods for granular media based on photoelastic theory is presented in [12]. Figure 2 shows a pattern of dark and bright fringes formed by illuminating photoelastic particles placed in between two polarizing filters. The intensity field $I(x, y)$ of the pattern depends on local stresses inside the particle. To be more precise, let us consider the stress tensor inside the particle:

$$\sigma(x, y) = \begin{pmatrix} \sigma_{xx}(x, y) & \sigma_{xy}(x, y) \\ \sigma_{xy}(x, y) & \sigma_{yy}(x, y) \end{pmatrix}.$$

We denote its eigenvalues (principal stresses) by:

$$\sigma_{\pm}(x, y) = \frac{1}{2} \left(\sigma_{xx}(x, y) + \sigma_{yy}(x, y) \pm \sqrt{(\sigma_{xx}(x, y) - \sigma_{yy}(x, y))^2 + 4\sigma_{xy}^2(x, y)} \right).$$

The intensity field exhibited by a particle is then given by:

$$I(x, y) = I_0 \sin^2 \frac{\pi(\sigma_+(x, y) - \sigma_-(x, y))hC(\lambda)}{\lambda}, \quad (1)$$

where h is the material thickness, λ is the wavelength of light, C is the stress optic coefficient dependent on λ , and I_0 is a normalization constant related to the intensity of the light. In this paper, we consider 8-bit grayscale digital images, $I_0 = 255$ and $hC(\lambda)/\lambda = 0.18$ to closely match the experimental images used for calibration in [29].

The stress tensor can be computed from the forces acting on the particle using elasticity theory [30, 31]. We briefly explain how the tensor is computed on a single particle while a detailed treatment in the case of three forces can be found in [32]. Due to the nature of the problem, we can suppose that the Saint-Venant's compatibility condition is satisfied, i.e., there are no gaps or overlaps in the material. In the absence of internal body forces, this condition can be formulated by the following equation:

$$\frac{\partial^2 \epsilon_{xx}}{\partial y^2} - 2 \frac{\partial^2 \epsilon_{xy}}{\partial x \partial y} + \frac{\partial^2 \epsilon_{yy}}{\partial x^2} = 0, \quad (2)$$

where ε is the strain tensor. To write the above equation in terms of stress we use the generalized Hooke's law that imposes the following linear strain stress relation:

$$\varepsilon_{xx} = \frac{\sigma_{xx} - \nu\sigma_{yy}}{E}, \quad \varepsilon_{yy} = \frac{\sigma_{yy} - \nu\sigma_{xx}}{E}, \quad \varepsilon_{xy} = \frac{(1 + \nu)\sigma_{xy}}{E}, \tag{3}$$

where ν is the Poisson's ratio and E is the Young's modulus. The fact that the particle is in mechanical equilibrium implies:

$$\begin{aligned} \frac{\partial\sigma_{xx}}{\partial x} + \frac{\partial\sigma_{xy}}{\partial y} &= 0, \\ \frac{\partial\sigma_{yy}}{\partial y} + \frac{\partial\sigma_{xy}}{\partial x} &= 0. \end{aligned} \tag{4}$$

To make sure that the stress tensor satisfies the equilibrium condition (4) we search for a solution in the form of the Airy stress function φ and express the components of the tensor σ as:

$$\sigma_{xx} = \frac{\partial^2 \varphi}{\partial y^2}, \quad \sigma_{yy} = \frac{\partial^2 \varphi}{\partial x^2}, \quad \sigma_{xy} = \frac{\partial^2 \varphi}{\partial x \partial y}. \tag{5}$$

By combining equations (3) and (5) we get an expression for the strain tensor in terms of φ . We substitute this expression into equation (2) and obtain the final equation:

$$\left(\frac{\partial^2}{\partial x^2} + \frac{\partial^2}{\partial y^2}\right) \left(\frac{\partial^2 \varphi}{\partial x^2} + \frac{\partial^2 \varphi}{\partial y^2}\right) = 0. \tag{6}$$

As is typical for partial differential equations we need to impose the correct boundary conditions. In our case, it is natural to require that there is no stress on the boundary of the particle except at the points where the external forces act on it.

To solve equation (6) we exploit the fact that its solution is well known for a semi-infinite plane with a single perpendicular force acting on it at some point O , see figure 3(a). Let us consider a polar coordinate system based in O with angles measured counterclockwise from the force vector. In this coordinate system, the Airy stress function is given by $\varphi(r, \theta) = \frac{F}{\pi h} r \theta \sin \theta$, where F is the magnitude of the force and h is the thickness of the plane. With this in mind, the stress tensor can be written as:

$$\sigma_{rr}(r, \theta) = -\frac{2F \cos \theta}{\pi h r}, \quad \sigma_{\theta\theta}(r, \theta) = 0, \quad \sigma_{r\theta}(r, \theta) = 0. \tag{7}$$

Now we turn our attention to an elastic disc exposed to M external forces. As indicated in figure 3(b), each of these forces can be encoded by a triplet (F_i, α_i, τ_i) . The value F_i is the magnitude of the i th force measured in Newtons. The impact point O_i of this force is determined by an impact angle α_i between the x -axis and the line connecting the center of the particle to O_i . Finally, τ_i is the angle between the direction of the force and the line segment $\overline{O_i C}$. The angles α_i and τ_i are measured counterclockwise in radians. The fact that equation (6) is linear makes it possible to compute the final stress $\sigma(x, y)$ by summing up the stresses $\sigma^i(x, y)$ caused by individual forces.

Inspired by the example of the semi-infinite plane, we seek the solution for the stress due to the force (F_i, α_i, τ_i) in the polar coordinates (r_i, θ_i) centered at the point O_i measuring the angle θ_i counterclockwise from the direction of the force, see figure 3(b). In this coordinates the stress σ^i can be written as:

$$\sigma_{r_i r_i}^i(r_i, \theta_i) = -\frac{2F_i \cos \theta_i}{\pi h r_i} + \frac{F_i}{\pi R h} \cos \tau_i, \quad \sigma_{\theta_i \theta_i}^i(r_i, \theta_i) = 0, \quad \sigma_{r_i \theta_i}^i(r_i, \theta_i) = 0, \tag{8}$$

where h is the thickness of the particle and R is its radius. The first term of $\sigma_{r_i r_i}^i(r_i, \theta_i)$ is analogous to the solution on the semi-infinite plane and the second term is added to ensure that the boundary condition (no stress except at the impact points) is satisfied. Note that each of the stress tensors σ^i is expressed in a different polar coordinate system. To obtain the full stress tensor $\sigma(x, y)$ in Cartesian coordinates we perform appropriate changes of coordinate systems as we sum up the individual stresses. So the total stress is:

$$\sigma(x, y) = \sum_{i=1}^M T(\theta_i(x, y)) \sigma^i(r_i(x, y), \theta_i(x, y)), \tag{9}$$

where the matrix $T(\theta)$ rotates the plane by the angle θ .

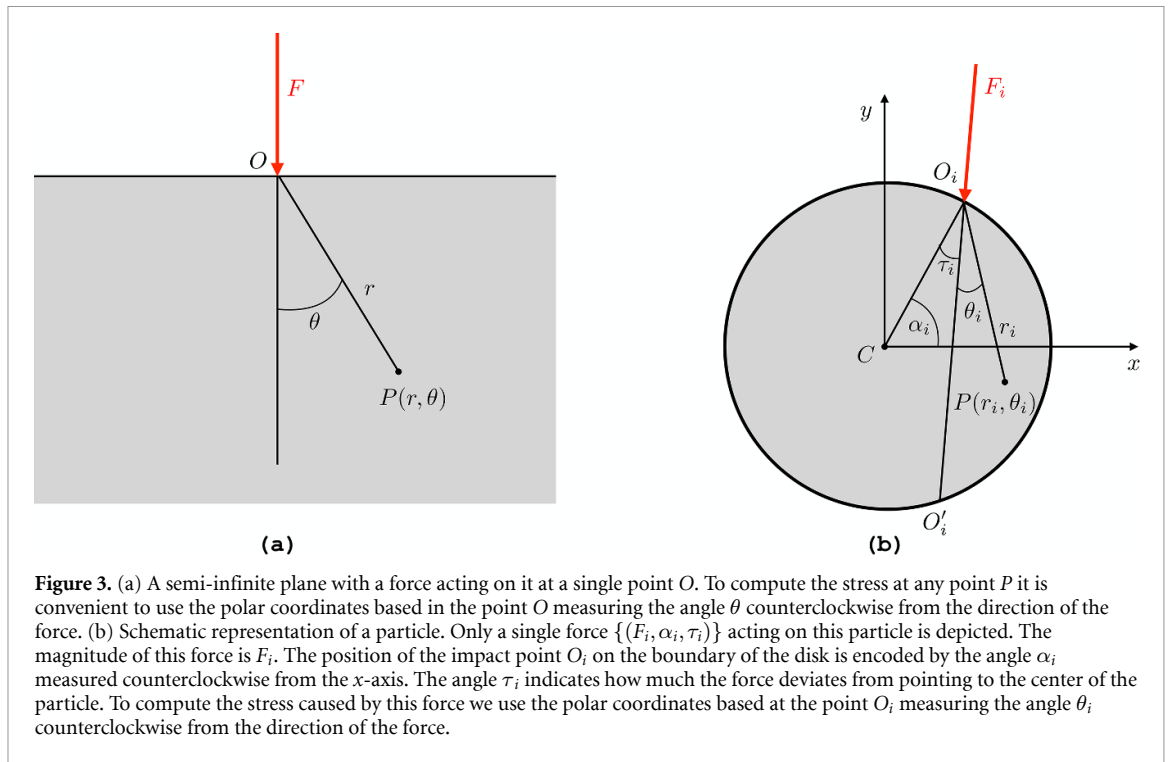


Figure 3. (a) A semi-infinite plane with a force acting on it at a single point O . To compute the stress at any point P it is convenient to use the polar coordinates based in the point O measuring the angle θ counterclockwise from the direction of the force. (b) Schematic representation of a particle. Only a single force $\{(F_i, \alpha_i, \tau_i)\}$ acting on this particle is depicted. The magnitude of this force is F_i . The position of the impact point O_i on the boundary of the disk is encoded by the angle α_i measured counterclockwise from the x -axis. The angle τ_i indicates how much the force deviates from pointing to the center of the particle. To compute the stress caused by this force we use the polar coordinates based at the point O_i measuring the angle θ_i counterclockwise from the direction of the force.

3. Force reconstruction from photoelastic response

In the previous section, we explained how to compute the photoelastic response of a circular particle if the forces acting on it are known. Extracting the forces acting on individual particles from experimental data is a much more complicated problem. Figure 1 is an example of an experimental image of the photoelastic patterns exhibited by a group of particles. This image is only shown to illustrate the patterns and cannot be directly used for the force reconstruction which requires monochromatic lighting of the particles.

There are several computational packages [14, 15] that implement the force reconstruction based on the technique pioneered in [3]. As explained in [12], these methods require two images of the same group of particles. The first image taken in unpolarized light is used to extract the positions of the particles and create a preliminary list of force-bearing contacts. This list of forces is then refined using the photoelastic patterns visible in the second image taken in polarized monochromatic light. For each particle, an initial list of forces acting at the force-bearing contacts is guessed based on a squared local gradient average of the pattern. Then, an optimization algorithm is used to minimize the L_2 difference between the experimentally captured pattern and the pattern generated from the reconstructed forces.

As indicated in [12], the positions of the particles can be computed with high accuracy using the Hough transform. On the other hand, we are not aware of any systematic study of the accuracy of the force reconstruction. In particular, reconstruction of the force acting between two particles can considerably vary depending on which of the two particles is used for the reconstruction [12]. Therefore, we consider the primary problem to be force reconstruction from the photoelastic response for the individual particles.

In this paper, we reconstruct the forces $\{(F_i, \alpha_i, \theta_i)\}_{i=1}^M$ acting on a particle by exploiting the natural constraints due to geometry and physical properties of the particles typically used in experiments. We summarize these constraints in the rest of this section.

In principle, there could be a large number of forces acting on a single particle but this is not the case if the sizes of particles in the ensemble do not vary too much, see figure 1. In this case, the number of forces acting on a particle may be assumed to be less than or equal to six. To avoid technicalities and demonstrate the ideas, we concentrate on bi-disperse particles. By simple modifications indicated in section 7, our method can be expanded to polydisperse materials. In the case of bi-disperse particles the impact points at which the forces act on the particle cannot be too close to each other. To be more precise, the angles α_i encoding positions of the impact points can be assumed to satisfy:

$$|\alpha_i - \alpha_j| \geq \frac{\pi}{6}, \text{ if } i \neq j. \quad (10)$$

The photoelastic theory presented in section 2 is only valid if the particles are in mechanical equilibrium. Thus, to ensure that the reconstruction works properly, particles have to be allowed to equilibrate before collecting the data. The fact that the particles are in a mechanical equilibrium imposes force balance and torque balance constraints on each particle. Moreover, the force balance on a particle implies that $M \geq 2$.

Finally, the friction coefficient μ of the particles is typically smaller than 1 and so the angles τ_i satisfy:

$$-\frac{\pi}{2} \leq \tau_i \leq \frac{\pi}{2}. \quad (11)$$

For example, the friction coefficient of the particles shown in figure 1 is $\mu = 0.8$ as reported in [13].

4. Machine learning approach to force reconstruction

In this section, we set up a machine learning framework for reconstructing the forces acting on a particle from its photoelastic response. We use CNNs in conjunction with transfer learning [33–36]. While CNNs are well suited for the recognition of spatial patterns in digital images [17, 21, 22], transfer learning yields outstanding results for a wide range of applications such as medical image analysis, speech emotion recognition, and quantum phase transition identification [37–40]. We utilize inductive transfer learning, in which a model originally trained to perform some (unrelated) task is retrained to carry out a new task. In section 6, we show that the previous knowledge helps the model to achieve high accuracy using a relatively small training set. Furthermore, in section 6, we demonstrate that the models trained on the synthetic data are likely to transfer reasonably well to the experimental data.

4.1. Pipeline architecture

A single CNN model to reconstruct the forces acting on a particle would have to be rather complex and contain many layers. Therefore, a large training set would be necessary to prevent overfitting. We avoid this problem by dividing the reconstruction of the force list $\{(F_i, \alpha_i, \tau_i)\}_{i=1}^M$ into four smaller tasks.

The first task is to infer the number M of the forces acting on the particle. For this purpose, we use a single CNN model. The reconstruction is then further divided into three additional tasks: inferring the magnitudes F_i , reconstructing the angles α_i , and finally estimating τ_i . As explained in section 3, we assume that $2 \leq M \leq 6$. Thus, for each of the three additional tasks we implement a collection of five independent CNN models. In other words, we use one model for each task and every possible value of M .

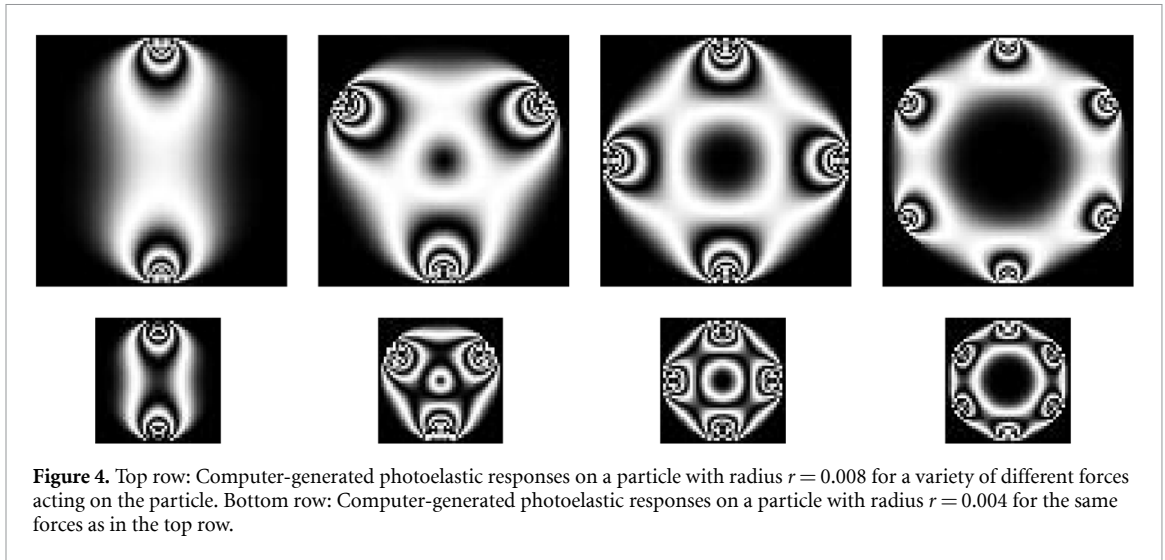
4.2. Models

We experimented with transfer learning for the individual tasks by using three models that show state-of-the-art performance on the benchmark data sets. In particular we considered the VGG19, InceptionResNetV2, and Xception models, pre-trained on the ImageNet data set [22–24]. The ImageNet data set is a benchmark data set which contains 3.9 million labeled images of real-world objects divided into 1000 distinct classes. The model VGG19 developed by [41] is an example of a traditional deep CNN, whose main power lies in its depth. On the other hand, InceptionResNetV2 is built upon the Inception architecture and further adds the residual connections to boost the performance as outlined in [23]. Finally, the Xception model is again based on the Inception architecture but replaces the Inception modules with depthwise separable convolutions [24].

To train the models on our data set, we remove the last fully connected layer for the Xception and InceptionResNetV2 models and the last three fully connected layers for the VGG19 model. Instead, we placed a global averaging layer followed by two dense layers with a 50% drop out in between them for the Xception and InceptionResNetV2 models. For the VGG19 model, we place a flattening layer again followed by two dense layers with a 50% drop out in between them. The first dense layer for all models is followed by ReLU activation. Depending on the task of the model we use either SoftMax or linear activation for the last dense layer, which is essentially the output layer.

5. Training of the neural networks

We train and test our models on the synthetic data generated using the algorithm described in section 2. Training the models on synthetic data can be desirable when the labeled experimental data is scarce. This strategy was already successfully used for the tasks of object detection, optical flow estimation, and scene understanding [25–27]. To assess the quality of the transfer learning, we test the models on smaller-sized particles. So we first train the models on particles with radius $r = 0.008$ and then take these pre-trained models and retrain them on particles with $r = 0.004$. Figure 4 shows that changing the radius of the particles alters the exhibited photoelastic patterns considerably. Thus a successful transfer between the particles of the



different sizes gives hope that the models would transfer well to the experimental data as well. Before discussing the training of different models we first summarize the protocol for generating the data sets used for training, validation, and testing purposes.

5.1. Generating the data sets

As explained in section 2, the photoelastic pattern on a particle can be computed from the list of forces $\{(F_i, \alpha_i, \tau_i)\}_{i=1}^M$ acting on it. To decrease the bias of the model the force lists in the training set must form a representative sample [42]. To ensure that the generated force lists are realistic we enforce the constraints presented in section 3. We require that forces and torques are balanced and the normal component of the force is larger than its tangential component, i.e. $|\tau_i| \leq \pi/2$. For bi-disperse systems, considered in this paper, we assume that $2 \leq M \leq 6$ and the angles of distinct impact points satisfy $|\alpha_i - \alpha_j| \geq \pi/6$.

To create a diverse training set with realistic forces we use the following procedure. For each value of M we create the same number of force lists. To construct a force list $\{(F_i, \alpha_i, \tau_i)\}_{i=1}^M$ we start by randomly generating the first $M - 1$ forces. The last force, described by (F_M, α_M, τ_M) , is then added to achieve force and torque balance. The angles:

$$\alpha_i \sim \mathcal{U}\left(\frac{2\pi(i-1)}{M} + \frac{\pi}{12}, \frac{2\pi i}{M} - \frac{\pi}{12}\right), \quad 1 \leq i \leq M-1, \quad (12)$$

are drawn from uniform distributions. The magnitudes of the first $M - 1$ forces are drawn from a normal distribution:

$$F_i \sim \mathcal{N}\left(F, \left(\frac{F}{5}\right)^2\right), \quad (13)$$

where F is sampled from the exponential distribution the rate parameter $1/2$ truncated to the interval $[0.01, 0.9]$. This distribution closely resembles the distribution obtained experimentally in [43]. Finally, each angle τ_i is taken from the normal distribution:

$$\tau_i \sim \mathcal{N}\left(0, \frac{\pi}{12}\right). \quad (14)$$

After producing a force list we check that all the assumed conditions from section 3 are satisfied. If these conditions are not satisfied, then we generate a new force list and discard the old.

For each accepted force list we produce a photoelastic pattern generated by this list. The resolution of the digital images depicting the patterns is 0.00019 meters per pixel for both small and larger particles. The data set for the particle with radius $r = 0.008$ contains 24000 distinct force lists (4800 for each possible value of M) accompanied by the corresponding photoelastic patterns. For the smaller particle, we generate a data set consisting of 7400 force lists (1480 for each possible value of M).

We split the generated data sets, for each value of M , randomly into the training, validation, and test sets as follows. For the large particle, we use 3200 samples for the training set, 800 for the validation set and the

test set. For the small particle, we create a sequence of three independent training sets with sizes 64, 160, 640 and three independent validation sets with sizes 16, 40, 160. The common test set contains 400 samples.

Separately, for each of the sets, we perform the following data augmentation to boost the generalization power of the models. We randomly rotate each sample 5 times using random angles drawn from the uniform distribution $\mathcal{U}(0, 2\pi)$. To achieve a uniform size of the image, we resize them to 128×128 pixels using the nearest neighbor interpolation. Finally, to ensure a natural look of the rotated images we apply Gaussian blur with standard deviation $\sigma = 1$ [44].

5.2. Training the models

We recall that our pipeline contains four units. The first classification unit infers the number of forces acting on the particle while the other three regression units reconstruct the individual components of the force list. As suggested in [42], we use the mean absolute error as a loss function for training the regression units. For the classification unit, we utilize one hot encoded vector to describe the probabilities that the object belongs to a particular class and employ the categorical cross-entropy as a loss function. For the optimization algorithm, we chose to use Adam optimizer [45], which is the default algorithm used to train all the models [22–24].

We start by training only the last fully connected block while freezing the rest of the model. This warm-up period is important because the weights for the new output block are initialized randomly. Skipping this step could corrupt the weights of the original pre-trained model, which are supposed to provide useful representations of the data [33]. To further decrease the chance of breaking the pre-trained model during its fine-tuning when all the weights are allowed to change, we decrease the learning rate from the standard value 10^{-3} to 10^{-6} as suggested in [35]. We set the number of epochs to 200 for the warm-up and 100 iterations for the main training. We further implement early stopping and best model selection. For the early stopping, we set the patience to 20, which means that if the error does not decrease for more than 20 iterations, the training is finished. The best model selection is implemented by only saving the best-performing model.

5.3. Training on a smaller particle

For the small particles, instead of retraining the models from scratch, we reuse the models trained on the larger-sized particles. To alleviate the computational burden, for each task we only consider the model with the best performance on the larger particle. As explained above, we use three pairs of train and validation sets with increasing sizes and one common test set. This is done to test the power of the transfer learning [33, 34]. In particular, we are interested in the size of the data set needed to achieve reasonable accuracy. By pairing each train set with a separate validation set, we prevent any possible data leakage. The common test set is used to measure the final accuracy of the whole model pipeline.

We train the models by leaving all the structural components intact and as before using the learning rate 10^{-6} because we are just fine-tuning the models. The tasks for the large and small particles are relatively similar, so we neither reprogram the top layer nor perform any warm-up [35].

6. Results

In this section, we demonstrate our results for reconstructing the forces acting on a particle from its photoelastic response. We start by comparing and contrasting the performance of the different models for the particle with radius $r = 0.008$.

Table 1 shows that the accuracy of detecting the number of forces acting on a particle is very high for all the models. Given the same time to train and similar training procedures, the VGG19 model marginally outperforms the other two. It is not only the high accuracy that makes our approach to detecting the number of forces appealing. Unlike the classical algorithms for detecting force-bearing contacts given in [12], our method does not require any adjustment of the parameters from the user. Since the misclassification is very rare, we test the subsequent models in the pipeline assuming that the number of forces acting on the particle is known.

Now we consider the accuracy of the reconstructed force lists $\{(F_i, \alpha_i, \tau_i)\}_{i=1}^M$. Figure 5 shows the mean absolute error (MAE) of the force magnitude, impact angle, and tangent angle for VGG19, Xception, and InceptionResNetV2 models. We report the errors separately for different values of M . The general trend is that the error increases with M . This could be caused by the fact that the patterns tend to be more complex for large values of M . The errors in the magnitude stay reasonably small for all considered models and values of M . This is not the case for the impact angle. The VGG19 shows much better performance than the other two models. The MAE of the VGG19 model is below three degrees for all values of M . This means that the mean error in detecting the impact point is around two pixels. The accuracy of the tangential angle reconstruction is much worse for all three models. For $M > 3$ it can reach 10 degrees. We expect that this is

Table 1. Accuracy of different models used for detecting the number of forces acting on a particle with radius $r = 0.008$.

Model	VGG19	Xception	InceptionResNetV2
Accuracy	0.9999	0.9835	0.9975

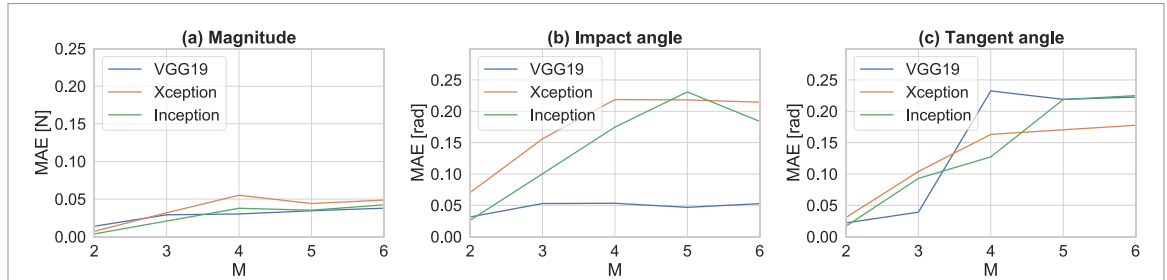


Figure 5. Mean absolute error (MAE) of the (a) force magnitude, (b) impact angle and (c) tangent angle for the particle with radius $r = 0.008$. Each panel shows the errors for VGG19, Xception, and InceptionResNetV2 models. We report the errors for each model and different numbers of forces, M , acting on a particle.

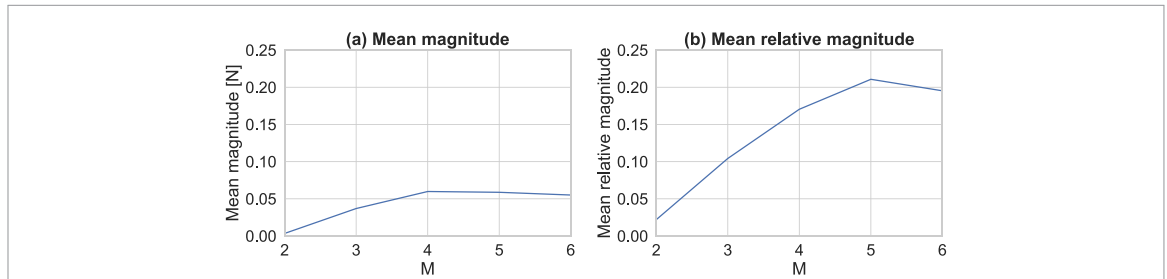


Figure 6. (a) Mean magnitude of the sum of the forces acting on a particle with radius $r = 0.008$. (b) Mean magnitude, shown in part (a), normalized by the average magnitude of the forces acting on the particle. We report the errors separately for different numbers of forces, M , acting on the particle.

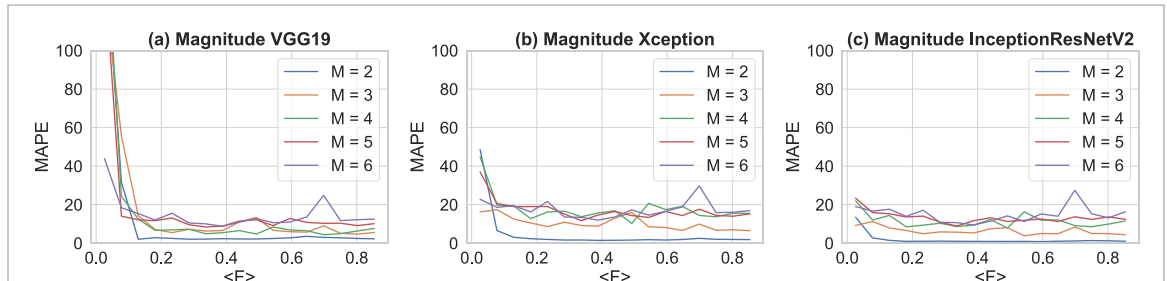


Figure 7. Dependence of the mean absolute percentage error (MAPE) on the average magnitude of the forces, $\langle F \rangle$, acting on the particle with radius $r = 0.008$. We report the errors separately for different numbers of forces, M , acting on a particle. The errors for different models are shown as follows (a) VGG19, (b) InceptionResNetV2 and (c) Xception.

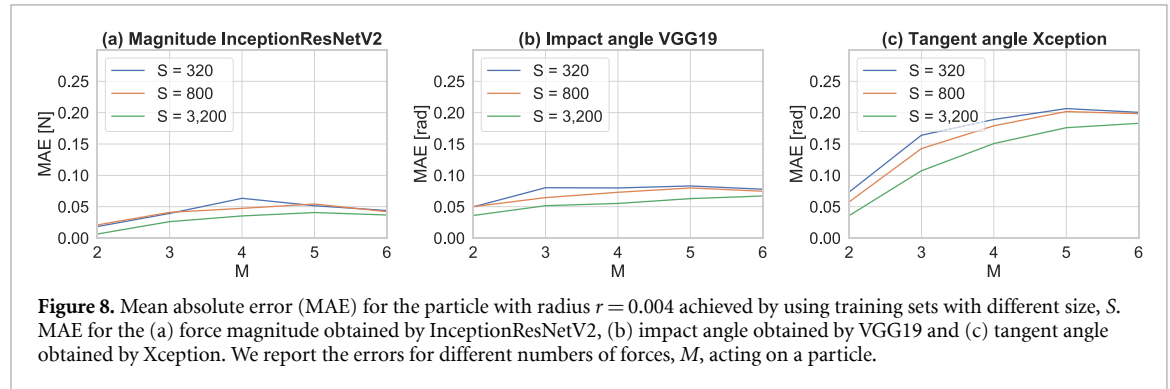
caused by the fact that changes of this angle have a less dramatic influence on the photoelastic pattern than the magnitude and impact angle.

We recall that the forces acting on the particle are required to be balanced. Hence, another more global way of accessing the quality of the reconstruction on a particle is to sum up the reconstructed forces. If the reconstruction works well the magnitude of the resulting vector \mathbf{v} should be small. Figure 6 shows that this is indeed the case. However, one can consider the magnitude of \mathbf{v} normalized by the average magnitude of the forces acting on the particle. As shown in figure 6, the mean of this quantity can be as large as 20% of the average magnitude. Upon further investigation, we have found out that the issue occurs if the magnitudes of the forces are relatively small. The classical methods exhibit the same problem and for this reason, the small forces are often disregarded [43].

To better understand the relative error of the force magnitude reconstruction we analyze its dependence on the average magnitude of the forces $\langle F \rangle$ acting on the particle. Figure 7 show how the MAPE changes with $\langle F \rangle$. As expected the relative error is typically larger for small values of $\langle F \rangle$. Figure 7 also shows that the InceptionResNetV2 model has the best performance.

Table 2. Accuracy of detecting the number of forces acting on a particle with radius $r = 0.004$ achieved by the VGG19 model trained on data sets with different sizes.

Size of the data set	320	800	3200
Accuracy	0.9828	0.9850	0.9884



Finally, we report how our models transfer to the particle with radius $r = 0.004$. Figure 4 shows that the same forces produce considerably different patterns depending on the particle size, but the nature of the patterns remains similar. Hence it is reasonable to expect that the models transfer well. To demonstrate this we only consider the best performing model for each task: VGG19 for detecting the number of forces and impact angle, InceptionResNetV2 for magnitudes, and Xception for tangent angle. Individual each model is retrained on independent data sets with increasing sizes $S = 320$, $S = 800$ and $S = 3200$.

Table 2 shows that the models achieve high accuracy of detecting the number of forces already on small data sets. Similarly figure 8 indicates that the force reconstruction accuracy comparable to the accuracy obtained on the large particle can be achieved on a much smaller data set. Similar analysis as performed for the larger particle shows that the relative magnitude error is larger if the average magnitude of the forces acting on the particle is small.

Differences between the patterns exhibited by the large and small particles exposed to the same forces, shown in figure 4, are quite considerable. This suggests a strong potential for using our models on the experimental data.

7. Conclusions

In this paper, we showed the strong potential of using CNNs for reconstructing forces acting between particles in photoelastic granular material. We compared the performance of the VGG19, Xception, and InceptionResNetV2 models. We conclude that some models work better than others for reconstructing particular components of the forces. However, to achieve the high accuracy of our predictions we had to train the models on a large labeled data set. Unfortunately, it is almost impossible to produce a data set of this size experimentally. Thus, we demonstrated that training on a large experimental data set could be avoided by first pretraining the models on a synthetic data set and then fine-tuning them on a much smaller set produced experimentally. We demonstrate the strength of this approach by showing that the models trained on a given particle transfer excellently to a smaller-sized particle and achieve high accuracy on a rather small training set.

For simplicity, we only considered bi-disperse granular materials. This assumption reduces the number of possible forces acting on an individual particle to six. However, in a particular experiment, the number of forces acting on a particle can be larger and the range of these forces can differ from our choice. In that case our model, available at [46], should be retrained using an appropriate synthetic data set before fine-tuning it to the experimental data. To ensure that the number of forces acting on each particle is detected properly, we suggest using a slightly broader range of forces than the range expected in the experiments.

One of the main advantages of using CNN is that after the models are trained the force reconstruction becomes extremely fast. Therefore, this approach can be used to analyze the time evolution of granular ensembles consisting of a large number of particles.

Finally, to expand our approach to polydisperse materials, used in a variety of experiments [3, 13, 43, 47], we propose first to split particles into groups with roughly the same radius. A separate set of models then

needs to be trained for each group. We showed that training additional models requires much less effort since we can use transfer learning.

Data availability statement

The data that support the findings of this study are available upon reasonable request from the authors.

Acknowledgments

The authors would like to thank C Colonnello and L Kondic for very useful comments on the manuscript. RS was supported by the Undergraduate Research Opportunity Program grant from the University of Oklahoma. MK was supported by a Junior Faculty Fellowship from the University of Oklahoma.

ORCID iDs

Renat Sergazinov  <https://orcid.org/0000-0001-5905-3674>

Miroslav Kramár  <https://orcid.org/0000-0001-7773-6516>

References

- [1] Duran J 2000 *Sands, Powders and Grains: An Introduction to the Physics of Granular Materials* (Berlin: Springer)
- [2] Bouchaud J, Claudin P, Cates M and Wittmer J 1998 Models of stress propagation in granular media *Physics of Dry Granular Media* (Berlin: Springer) pp 97–122
- [3] Majmudar T S and Behringer R P 2005 Contact force measurements and stress-induced anisotropy in granular materials *Nature* **435** 1079
- [4] Clark A H, Petersen A J, Kondic L and Behringer R P 2015 Nonlinear force propagation during granular impact *Phys. Rev. Lett.* **114** 144502
- [5] Falcon E, Castaing B and Creyssels M 2004 Nonlinear electrical conductivity in a 1d granular medium *Euro. Phys. J. B* **38** 475–83
- [6] Dorbolo S and Vandewalle N 2002 Electrical investigations of granular arches *Physica A* **311** 307–12
- [7] Jia X, Caroli C and Velicky B 1999 Ultrasound propagation in externally stressed granular media *Phys. Rev. Lett.* **82** 1863
- [8] Makse H A, Gland N, Johnson D J and Schwartz L M 2004 Granular packings: nonlinear elasticity, sound propagation and collective relaxation dynamics *Phys. Rev. E* **70** 061302
- [9] Lherminier S, Planet R, Simon G, Vanel L and Ramos O 2014 Revealing the structure of a granular medium through ballistic sound propagation *Phys. Rev. Lett.* **113** 098001
- [10] Wakabayashi T 1950 Photoelastic method for determination of stress in powdered mass *J. Phys. Soc. Japan* **5** 383–5
- [11] Dantu P 1957 *Proc. 4th Int. Conf. on Soil Mechanics and Foundations Engineering* (London: Butterworths Scientific Publications)
- [12] Daniels K E, Kollmer J E and Puckett J G 2017 Photoelastic force measurements in granular materials *Rev. Sci. Instrum.* **88** 051808
- [13] Wang D, Ren J, Dijkstra J A, Zheng H and Behringer R P 2018 Microscopic origins of shear jamming for 2d frictional grains *Phys. Rev. Lett.* **120** 208004
- [14] Puckett J Photoelastic disk solver (pediscolve) (available at: <http://nile.physics.ncsu.edu/pub/download/peDiscSolve/>)
- [15] Kollmer J Photoelastic grain solver (pegs) (available at: <https://github.com/jekollmer/PEGS>)
- [16] Bishop C M 2006 *Pattern Recognition and Machine Learning* (Berlin: Springer)
- [17] LeCun Y, Bengio Y and Hinton G 2015 Deep learning *Nature* **521** 436–44
- [18] Bacacier L, Barnard E, Karpov A and Schultz T 2014 Automatic speech recognition for under-resourced languages: a survey *Speech Commun.* **56** 85–100
- [19] Chorowski J and Jaitly N 2016 Towards better decoding and language model integration in sequence to sequence models (arXiv:1612.02695)
- [20] Jiao L, Zhang F, Liu F, Yang S, Li L, Feng Z and Qu R 2019 A survey of deep learning-based object detection *IEEE Access* **7** 128837–68
- [21] Krizhevsky A, Sutskever I and Hinton G E 2012 Imagenet classification with deep convolutional neural networks *Advances in Neural Information Processing Systems* vol 25 pp 1097–105
- [22] Simonyan K and Zisserman A 2015 Very deep convolutional networks for large-scale image recognition (arXiv:1409.1556)
- [23] Szegedy C, Ioffe S, Vanhoucke V and Alemi A 2017 Inception-V4, Inception-Resnet and the impact of residual connections on learning *Proc. Conf. Artificial Intelligence* vol **31**
- [24] Chollet F 2017 Xception: deep learning with depthwise separable convolutions *Proc. Conf. Computer Vision and Pattern Recognition* pp 1251–8
- [25] Tremblay J *et al* 2018 Training deep networks with synthetic data: bridging the reality gap by domain randomization *Proc. Conf. Computer Vision and Pattern Recognition Workshops* pp 969–77
- [26] Handa A, Patraucean V, Badrinarayanan V, Stent S and Cipolla R 2015 Scenenet: understanding real world indoor scenes with synthetic data (arXiv:1511.07041)
- [27] Mayer N, Ilg E, Hausser P, Fischer P, Cremers D, Dosovitskiy A and Brox T 2016 A large dataset to train convolutional networks for disparity, optical flow and scene flow estimation *Proc. Conf. Computer Vision and Pattern Recognition* pp 4040–8
- [28] Frocht M 1941 *Photoelasticity* vol 1 (New York: Wiley)
- [29] Majmudar T S 2006 Experimental studies of two-dimensional granular systems using grain-scale contact force measurements *PhD Thesis* Duke University
- [30] Landau L 1986 *Theory of Elasticity: Volume 7 (Course of Theoretical Physics)* 3rd edn (Oxford: Butterworth-Heinemann)
- [31] Love A E H 2013 *A Treatise on the Mathematical Theory of Elasticity* (Cambridge: Cambridge University Press)
- [32] Chau M 2018 Analyzing 3-point symmetric contacts of photoelastic disks *PhD Thesis* Reed College
- [33] Pan S J and Yang Q 2009 A survey on transfer learning *IEEE Trans. Knowl. Data Eng.* **22** 1345–59

- [34] Zhuang F, Qi Z, Duan K, Xi D, Zhu Y, Zhu H, Xiong H and He Q 2020 A comprehensive survey on transfer learning *Proc. IEEE* **109** 43–76
- [35] Yosinski J, Clune J, Bengio Y and Lipson H 2014 How transferable are features in deep neural networks? *Advances in Neural Information Processing Systems* vol 27 pp 3320–8
- [36] Sharif Razavian A, Azizpour H, Sullivan J and Carlsson S 2014 CNN features off-the-shelf: an astounding baseline for recognition *Proc. Conf. Computer Vision and Pattern Recognition Workshops* pp 806–13
- [37] Shin H C, Roth H R, Gao M, Lu L, Xu Z, Nogues I, Yao J, Mollura D and Summers R M 2016 Deep convolutional neural networks for computer-aided detection: CNN architectures, dataset characteristics and transfer learning *IEEE Trans. Med. Imaging* **35** 1285–98
- [38] Tajbakhsh N, Shin J Y, Gurudu S R, Hurst R T, Kendall C B, Gotway M B and Liang J 2016 Convolutional neural networks for medical image analysis: full training or fine tuning? *IEEE Trans. Med. Imaging* **35** 1299–1312
- [39] Deng J, Zhang Z, Eyben F and Schuller B 2014 Autoencoder-based unsupervised domain adaptation for speech emotion recognition *IEEE Signal Process. Lett.* **21** 1068–72
- [40] Huembeli P, Dauphin A and Wittek P 2018 Identifying quantum phase transitions with adversarial neural networks *Phys. Rev. B* **97** 134109
- [41] Simonyan K and Zisserman A 2014 Very deep convolutional networks for large-scale image recognition (arXiv:1409.1556)
- [42] Chollet F 2017 *Deep Learning With Python* (New York: Manning Publications Company)
- [43] Dijkstra J A, Kovalcinova L, Ren J, Behringer R P, Kramár M, Mischenko K and Kondic L 2018 Characterizing granular networks using topological metrics *Phys. Rev. E* **97**
- [44] Goodfellow I, Bengio Y, Courville A and Bengio Y 2016 *Deep Learning* vol 1 (Cambridge: MIT Press)
- [45] Kingma D and Ba J 2014 Adam: a method for stochastic optimization (arXiv:1412.6980)
- [46] Sergazinov R and Kramár M 2020 (available at: <https://github.com/mrsergazinov/particle-force-cnn>)
- [47] Tordesillas A, Walker D M, Froyland G, Zhang J and Behringer R P 2012 Transition dynamics and magic-number-like behavior of frictional granular clusters *Phys. Rev. E* **86** 011306